LCAO Xα Calculation of the Magnetic Exchange Interactions in a $Mn^{IV}Mn^{III}_3$ Cubane Complex: Relevance to the Water Oxidation Center of Photosystem II

Edward A. Schmitt,[1] Louis Noodleman,*[,2] Evert Jan Baerends,[3] and David N. Hendrickson*[,1]

Contribution from the Department of Chemistry 0506, University of California at San Diego, La Jolla, California 92093-0506, Department of Molecular Biology, The Scripps Research Institute, La Jolla, California 92037, and Scheikundig Laboratorium, Vrije Universiteit, De Boelelaan 1083, 1081 HV Amsterdam, The Netherlands. *Received October 25, 1991*

Abstract: The results of density functional calculations of the LCAO Xα type which employed the broken symmetry method are presented for the experimentally known distorted cubane complex $[Mn^{IV}Mn^{III}_3O_3Cl_7(O_2CCH_3)_3]^{3-}$, complex **1**. Of all the spin states possible, the ground state was calculated to have $S = {}^9/_2$, in agreement with magnetic susceptibility results. Magnetic exchange parameters ($-2J_{ij}\hat{S}_i\hat{S}_j$ Hamiltonian) characterizing the Mn^{III}–Mn^{III} (J_{33}) and Mn^{III}–Mn^{IV} (J_{34}) interactions were calculated. Values of $J_{33} = 19.3$ cm^{-1}(ferromagnetic) and $J_{34} = -46.6$ cm^{-1} (antiferromagnetic) were calculated employing the Xα potential with Becke gradient energy and the larger basis set. These values are comparable to exchange parameters experimentally evaluated from susceptibility data for similar $Mn^{IV}Mn^{III}_3O_3Cl$ cubane complexes. Net charge and spin densities were also calculated for the three ($M_s = {}^{15}/_2, {}^9/_2$, or ${}^1/_2$) broken symmetry states. From the calculated net charges and compositions of molecular orbitals it is clear that for most molecular orbitals there is extensive mixing of metal and ligand atomic orbitals. Only small changes in atomic charges are found for the three broken symmetry states. From the net spin densities it was found that the μ_3-Cl atom is a net β spin donor toward the three Mn^{III} atoms. On the other hand the three μ_3-O atoms are net β spin donors to the Mn^{IV} ion, and with respect to the Mn^{III} ions, they are net α spin donors. An analysis is presented to show that spin polarization of the bridging and terminal ligands is likely the major contributor to the metal–metal spin coupling. There are probably cooperative effects among the different ligands with respect to spin donation with corresponding effects on the magnitude of the pairwise magnetic exchange interactions in $[Mn_4O_3Cl_7(O_2CCH_3)_3]^{3-}$. A comparison of the nature and origin of exchange interactions and ground states is made between the Mn_4 complex **1** and reduced $Fe_4S_4^{1+}$ and $Fe_4Se_4^{1+}$ complexes.

Introduction

The magnitude and nature of pairwise magnetic exchange interactions determine the ground and low-lying excited states in many polynuclear metal complexes. The distribution of electronic states is potentially important in determining the reactivities of these polynuclear complexes. It is of interest to note that electron-transport proteins with the $[Fe_4S_4(SR)_4]^{3-}$ active site have been reported[4] to have either $S = {}^1/_2, {}^3/_2, {}^5/_2$, or even larger spin ground states, a phenomenon which has also been well documented[5] for $[Fe_4S_4(SR)_4]^{3-}$ model complexes. Thus, even though magnetic exchange interactions are generally weak, it is important to understand them in detail. A considerable data base of exchange interaction parameters, i.e., J in the Heisenberg–Dirac–van Vleck spin Hamiltonian $-2J\hat{S}_i\cdot\hat{S}_j$, is available[6] from measurements on several complexes. A qualitative understanding of whether a given pairwise interaction is antiferromagnetic or ferromagnetic and the magnitude of an interaction are available in terms of the overlap of "magnetic orbitals".[7] However, there have been few quantum mechanical calculations[8-17] of magnetic exchange parameters.

There are several possible computational methodologies for performing quantum mechanical calculations on transition metal complexes. The problem of magnetic exchange interactions has only been examined to a limited extent compared to other electronic structural problems. Certainly the classic metal complex

(1) University of California at San Diego.
(2) The Scripps Research Institute.
(3) Vrije Universiteit.
(4) (a) Carney, M. J.; Papaefthymiou, G. C.; Spartalian, K.; Frankel, R. B.; Holm, R. H. *J. Am. Chem. Soc.* **1988**, *110*, 6084–6095 and references therein. (b) Carney, M. J.; Papaefthymiou, G. C.; Whitener, M. A.; Spartalian, K.; Frankel, R. B.; Holm, R. H. *Inorg. Chem.* **1988**, *27*, 346–352.
(5) (a) Huynh, B. H.; Henzl, M. T.; Christner, J. A.; Zimmerman, R.; Orme-Johnson, W. H.; Münck, E. *Biochim. Biophys. Acta* **1980**, *623*, 124. (b) Johnson, M. K.; Thomson, A. J.; Robinson, A. E.; Smith, B. E. *Biochim. Biophys. Acta* **1981**, *671*, 61. (c) Smith, J. P.; Emptage, M. H.; Orme-Johnson, W. H. *J. Biol. Chem.* **1982**, *257*, 2310. (d) Moringstar, J. E.; Johnson, M. K.; Case, E. E.; Hales, B. J. *Biochemistry* **1987**, *26*, 1795. (e) Vollmer, S. J.; Switzer, R. L.; Debrunner, P. G. *J. Biol. Chem.* **1983**, *258*, 14284. (f) Rusnak, F. M.; Adams, M. W. W.; Mortenson, L. E.; Münck, E. *J. Biol. Chem.* **1987**, *262*, 38. (g) Morgan, T. V.; Prince, R. C.; Mortenson, L. E. *FEBS Lett.* **1986**, *206*, 4. (h) Hagen, W. R.; Wassink, H.; Eady, R. R.; Smith, B. E.; Haaker, H. *Eur. J. Biochem.* **1987**, *169*, 457. (i) McLean, P. A.; Papaefthymiou, V.; Orme-Johnson, W. H.; Münck, E. *J. Biol. Chem.* **1987**, *262*, 12900. (j) Bertrand, P.; Gayda, J.-P.; Rao, K. K. *J. Chem. Phys.* **1982**, *76*, 4715. (k) Middleton, P.; Dickson, D. P. E.; Johnson, C. E.; Rush, J. D. *Eur. J. Biochem.* **1978**, *88*, 135. (l) Christner, J. A.; Münck, E.; Janik, P. A.; Siegel, L. M. *J. Biol. Chem.* **1981**, *256*, 2098. (m) Auric, P.; Gaillard, J.; Meyer, J.; Moulis, J.-M. *Biochem. J.* **1987**, *242*, 525. (n) Lindahl, P. A.; Day, E. P.; Kent, T. A.; Orme-Johnson, W. H.; Münck, E. *J. Biol. Chem.* **1985**, *260*, 11160. (o) Lindahl, P. A.; Gorelick, N. J.; Münck, E.; Orme-Johnson, W. H. *J. Biol. Chem.* **1987**, *262*, 14945.
(6) (a) *Theory and Applications of Molecular Paramagnetism*; Boudreaux, E. A., Mulay, L. N., Eds.; Wiley and Sons: New York, 1976. (b) Carlin, R. L. *Magnetochemistry*; Springer-Verlag: New York, 1986.
(7) *Magneto-Structural Correlation in Exchange-Coupled Systems*; Willett, R. D., Gatteschi, D., Kahn, O., Eds.; NATO ASI Series C, 140; D. Reidel Publishing Co.: Dordrecht, Holland, 1985.
(8) Charlot, M.-F.; Verdaguer, M.; Journaux, Y.; de Loth, P.; Daudey, J. P. *Inorg. Chem.* **1984**, *23*, 3802–3808.
(9) Charlot, M.-F.; Kahn, O.; Chaillet, M.; Larrieu, C. *J. Am. Chem. Soc.* **1986**, *108*, 2574–2581.
(10) de Loth, P.; Karafiloglou, P.; Daudey, J.-P.; Kahn, O. *J. Am. Chem. Soc.* **1988**, *110*, 5676–5680.
(11) (a) Nepveu, F.; Haase, W.; Astheimer, H. *J. Chem. Soc., Faraday Trans.* **1986**, *82*, 551–565. (b) Astheimer, H.; Haase, W. *J. Chem. Phys.* **1986**, *85*, 1427–1432.
(12) de Loth, P.; Cassoux, P.; Daudey, J. P.; Mabieu, J. P. *J. Am. Chem. Soc.* **1981**, *103*, 4007–4016.
(13) Yamaguchi, K.; Fueno, T.; Ueyama, N.; Nakamura, A.; Ozaki, M. *Chem. Phys. Lett.* **1989**, *164*, 210–216.
(14) Yamaguchi, K.; Tsunekawa, T.; Toyoda, Y.; Fueno, T. *Chem. Phys. Lett.* **1988**, *143*, 371–376.
(15) Hay, P. J.; Thibeault, J. C.; Hoffmann, R. *J. Am. Chem. Soc.* **1975**, *97*, 4884–4899.
(16) (a) Ross, P. K.; Solomon, E. I. *J. Am. Chem. Soc.* **1990**, *112*, 5871. (b) Ross, P. K.; Solomon, E. I. *J. Am. Chem. Soc.* **1991**, *113*, 3246.
(17) (a) Bencini, A.; Gatteschi, D. *J. Am. Chem. Soc.* **1986**, *108*, 5763. (b) Bencini, A. *J. Chim. Phys. Phys.-Chim. Biol.* **1989**, *86*, 763.

0002-7863/92/1514-6109$03.00/0

in the realm of magnetic exchange interactions is the copper acetate dimer, $[Cu(O_2CCH_3)_4(H_2O)]_2$. Ballhausen and Forster[18] in 1962 employed a Hückel molecular orbital calculation to devise a one-electron orbital scheme to implicate a copper–copper σ bond. Later calculations[19] indicated that there was not a direct copper–copper interaction and that configuration interaction is necessary to calculate the exchange interaction ($2J = -294 \pm 4$ cm^{-1} is the separation between the singlet and triplet states[20]). The most recent theoretical interpretations of the exchange interaction in the copper acetate dimer hydrate include angular overlap calculations by Gerloch and Harding[21] and the iterative extended Hückel calculations of Hoffmann et al.[15] and Kahn et al.[22] Presently the exchange interaction in the copper acetate dimer is believed to result from a superexchange pathway involving the acetates. Unfortunately such a simplified technique as the extended Hückel molecular orbital calculation cannot be expected to give quantitative evaluations of magnetic exchange interactions.[23]

The most thorough calculation of J for the copper acetate dimer hydrate was reported by de Loth et al.[12] An all-electron ab initio SCF-MO calculation was completed employing a contracted set of Gaussian orbitals. The SCF calculation of the singlet state gives an antisymmetrical combination of the $d_{x^2-y^2}$ copper orbital for the lowest unoccupied molecular orbital (LUMO), whereas the highest occupied molecular orbital (HOMO) is the corresponding symmetric combination of $d_{x^2-y^2}$ orbitals. With their ab initio SCF-MO calculation as a zero point, de Loth et al. used perturbation theory to treat the configuration interaction (CI) required to evaluate the J parameter. They calculated a value of $2J$ between -90 and -214 cm^{-1}, the exact value depending on the choice of the perturbation treatment. CI to higher order than second was necessary for convergence.

The ab initio SCF plus CI approach has also been used to calculate J values for other Cu^{II}_2 complexes with azide[9] and oxalate[8] bridging groups. The ferromagnetic coupling in $[CuVO(fsa)_2en(CH_3OH)]$, where $[(fsa)_2en]^{4-}$ is a dinucleating ligand, was also calculated by de Loth et al.[10] In this $Cu^{II}\cdots V^{IV}$ complex the two unpaired electrons are in orthogonal orbitals, one on each metal ion. The calculated J value (343 cm^{-1}) was found to be more positive (ferromagnetic) than the reported experimental value (120 cm^{-1}). Finally, Haase's group has also employed the ab initio SCF plus CI approach to calculate exchange parameters for aromatic N-oxide bridged Cu^{II} dimers as well as bridge angle and Cu–O distance dependence of J in a series of $Cu^{II}_2O_2$ complexes.[11]

Many interesting magnetic exchange problems exist for complexes of nuclearity greater than 2 (i.e., trimers, tetramers, etc.) and with single-ion spins greater than $S = {}^1/_2$. The ab initio SCF plus CI technique is not readily applied to these complexes. The use of broken symmetry theory[24] in conjunction with ab initio methods can treat such complexes. Yamaguchi et al.[14] have used ab initio methods and broken symmetry theory to study exchange interactions in hypothetical M_2, M–O–M, and XM–O–MX complexes, where M is Cr^{III}, Mn^{II}, Fe^{III}, Cu^{II}, or Ni^{II}. The calculated J values for these hypothetical (simplified) complexes were found to be in the range found experimentally for related complexes.

Density functional methods[25] provide an effective theoretical method for examining the electronic structure of polynuclear metal complexes when combined with the concept of broken symmetry. Both spin-restricted[26] and spin-unrestricted[27] density functional calculations of the Xα type have been carried out for model complexes of the active sites of iron–sulfur proteins containing one, two, three, or four iron ions. The results of these calculations have given insight about the electronic structure of the protein active sites.[28] The Xα calculations provide an explanation for why $Fe^{III}\cdots Fe^{III}$ exchange interactions are of the order of 300–500 cm^{-1} in these Fe_nS_m complexes, whereas $Fe^{II}\cdots Fe^{III}$ and $Fe^{II}\cdots Fe^{II}$ interactions are appreciably less antiferromagnetic. From the results it is also possible to map out in a given iron–sulfur complex changes in charge and spin densities which occur as a given complex is oxidized or reduced by one electron.

In addition to iron–sulfur proteins there are many other proteins which have polynuclear metal sites where magnetic exchange interactions are important in determining the electronic structure. Polynuclear complexes which exhibit very weak exchange interactions ($|J| = 0$–50 cm^{-1}) present a challenge for quantum mechanical calculations. In this paper the spin-polarized density functional Xα and broken symmetry methodologies are employed to calculate the ground-state and magnetic exchange interactions for $[Mn_4O_3Cl_7(O_2CCH_3)_3]^{3-}$, complex **1**. The X-ray structure of the pyridinium salt shows that this anion has a distorted $Mn^{IV}Mn^{III}_3O_3Cl$ cubane core.[29] The S_2 state of the water oxidation center of photosystem II is believed to have a $Mn^{IV}Mn^{III}_3$ active site.[30] Two different EPR signals, one a multiline $g = 2$ signal and the other a $g = 4.1$ signal, have been detected for the S_2 state.[31] From recent work[32] it was concluded that these two EPR signals arise from two different conformations of a single tetranuclear manganese site, as suggested by Brudvig et al.[33] The $Mn^{IV}Mn^{III}_3$ site has a $S = {}^1/_2$ ground state ($g = 2$), and in one

(18) Forster, L. S.; Ballhausen, C. J. *Acta Chem. Scand.* **1962**, *16*, 1385–1392.
(19) Hansen, A. E.; Ballhausen, C. J. *Trans. Faraday Soc.* **1965**, *61*, 631–639.
(20) Güdel, H. U.; Stebler, A.; Furrer, A. *Inorg. Chem.* **1979**, *18*, 1021–1023.
(21) Gerloch, M.; Harding, J. H. *Proc. R. Soc. London* **1978**, *A360*, 211–227.
(22) Kahn, O.; Briat, B. *J. Chem. Soc., Faraday Trans.* **1976**, 268–281.
(23) Haddad, M. S.; Hendrickson, D. N.; Cannady, J. P.; Drago, R. S.; Bieksza, D. S. *J. Am. Chem. Soc.* **1979**, *101*, 898.
(24) (a) Noodleman, L.; Norman, J. G. *J. Chem. Phys.* **1979**, *70*, 4903. (b) Noodleman, L. *J. Chem. Phys.* **1981**, *74*, 5737. (c) Noodleman, L.; Davidson, E. R. *Chem. Phys.* **1986**, *109*, 131. (d) Noodleman, L.; Case, D. A. *Adv. Inorg. Chem.* **1992**, *38*, 423. (e) Ziegler, T.; Rauk, A.; Baerends, E. J. *Theor. Chim. Acta* **1977**, *43*, 261. (f) Lowdin, P. O. *Rev. Mod. Phys.* **1962**, *34*, 80. (g) Lowdin, P. O. *Rev. Mod. Phys.* **1962**, *34*, 520. (h) Lowdin, P. O. *Phys. Rev.* **1955**, *97*, 1509. (i) Benard, M. *J. Chem. Phys.* **1979**, *71*, 2546. (j) Benard, M.; Paldus, J. *J. Chem. Phys.* **1980**, *72*, 6546. (k) Fukotome, H. *Prog. Theor. Phys.* **1972**, *47*, 1156.
(25) *Density Functional Methods in Chemistry*; Labanowski, J. K., Andzelm, J. W., Eds.; Springer-Verlag: New York, 1991.
(26) (a) Yang, C. Y.; Johnson, K.; Holm, R. H.; Norman, J. G., Jr. *J. Am. Chem. Soc.* **1975**, *47*, 6596. (b) Norman, J. G., Jr.; Kalbacher, B. J.; Jackels, S. C. *J. Chem. Soc., Chem. Commun.* **1978**, 1027. (c) Geurts, P. J. M.; Gosselink, J. W.; van der Avoird, A.; Baerends, E. J.; Snijders, J. G. *Chem. Phys.* **1980**, *46*, 133.
(27) (a) Norman, J. G., Jr.; Jackels, S. C. *J. Am. Chem. Soc.* **1975**, *97*, 3833. (b) Norman, J. G., Jr.; Ryan, P. B.; Noodleman, K. *J. Am. Chem. Soc.* **1980**, *102*, 4279. (c) Aizman, A.; Case, D. A. *J. Am. Chem. Soc.* **1982**, *104*, 3269. (d) Noodleman, L.; Norman, J. G., Jr.; Osborne, J. H.; Aizman, A.; Case, D. A. *J. Am. Chem. Soc.* **1985**, *107*, 3418. (e) Noodleman, L. *Inorg. Chem.* **1988**, *27*, 3677. (f) Noodleman, L.; Aizman, A.; Case, D. A. *J. Am. Chem. Soc.* **1988**, *110*, 1001. (g) Noodleman, L.; Case, D. A.; Sontum, S. F. *J. Chim. Phys. Phys.-Chim. Biol.* **1989**, *86*, 743. (h) Sontum, S. F.; Noodleman, L.; Case, D. A. *The Challenge of d and f Electrons*; Salahub, D., Zerner, M. C., Eds.; American Chemical Society: Washington, DC, 1989; p 366. (i) Noodleman, L.; Baerends, E. J. *J. Am. Chem. Soc.* **1984**, *106*, 2316.
(28) Noodleman, L.; Case, D. A.; Baerends, E. J., chapter 8 in ref 25.
(29) Libby, E.; Schmitt, E. A.; Tsai, H.-L.; Christou, G.; Hendrickson, D. N. Unpublished results.
(30) For some recent reviews, see: (a) Brudvig, G. W.; Beck, W. F.; de Paula, J. C. *Annu. Rev. Biophys. Biophys. Chem.* **1989**, *18*, 25. (b) Brudvig, G. W.; Crabtree, R. H. *Prog. Inorg. Chem.* **1988**, *37*, 99. (c) Weighardt, K. *Angew. Chem., Int. Ed. Engl.* **1989**, 1153. (d) Christou, G. *Acc. Chem. Res.* **1989**, *22*, 328–335. (e) Pecoraro, V. L. *Photochem. Photobiol.* **1988**, *48*, 249. (f) Dismukes, G. C. *Chem. Scripta* **1988**, *28A*, 99–104.
(31) (a) Dismukes, G. C.; Siderer, Y. *Proc. Natl. Acad. Sci. U.S.A.* **1981**, *78*, 274–278. (b) Hansson, Ö.; Andréasson, L.-E. *Biochem. Biophys. Acta* **1982**, *679*, 261–268. (c) Casey, J. L.; Sauer, K. *Biochim. Biophys. Acta* **1984**, *767*, 21–28. (d) Zimmermann, J. L.; Rutherford, A. W. *Biochim. Biophys. Acta* **1984**, *767*, 160–167. (e) Hansson, Ö.; Aasa, R.; Vänngard, T. *Biophys. J.* **1987**, *51*, 825–832. (f) Zimmermann, J. L.; Rutherford, A. W. *Biochemistry* **1986**, *25*, 4609–4615.
(32) Kim, D. H.; Britt, R. D.; Klein, M. P.; Sauer, K. *J. Am. Chem. Soc.* **1990**, *112*, 9389–9391.
(33) (a) de Paula, J. C.; Brudvig, G. W. *J. Am. Chem. Soc.* **1985**, *107*, 2643–2648. (b) de Paul, J. C.; Beck, W. F.; Brudvig, G. W. *J. Am. Chem. Soc.* **1986**, *108*, 4002–4009. (c) de Paula, J. C.; Beck, W. F.; Miller, A.-F.; Wilson, R. B.; Brudvig, G. W. *J. Chem. Soc., Faraday Trans. 1* **1987**, *83*, 3635–3651. (d) Beck, W. F.; Brudvig, G. W. *Biochemistry* **1986**, *25*, 6479–6486. (e) de Paula, J. C.; Innes, J. B.; Brudvig, G. W. *Biochemistry* **1985**, *24*, 8114–8120. (f) Brudvig, G. W. In *Advanced EPR, Applications in Biology and Biochemistry*; Hoff, A. J., Ed.; Elsevier: Amsterdam, 1989; pp 839–865.

Table I. Selected Bond Lengths and Angles for $[Mn_4O_3(O_2CCH_3)_3Cl_7]^{3-}$ (**1**)[a]

Bond Lengths[b]			
Mn^{III}–μ_3-O	1.97	Mn^{III}–O(Ac)	2.16
Mn^{IV}–μ_3-O	1.87	Mn^{IV}–O(Ac)	1.97
Mn^{III}–μ_3-Cl	2.65	Mn^{III}–Cl	2.27
Mn^{III}···Mn^{IV}	2.84	Mn^{III}···Mn^{III}	3.34
Bond Angles[c]			
Mn^{III}–μ_3-O–Mn^{III}	115.55	μ_3-O–Mn^{III}–μ_3-O	80.15
Mn^{III}–μ_3-Cl–Mn^{III}	77.90	μ_3-O–Mn^{IV}–μ_3-O	85.56
Mn^{IV}–μ_3-O–Mn^{III}	95.20		

[a] The coordinates used in the calculations were obtained by symmetrizing (C_3 symmetry) the coordinates for $[Mn_4O_3(O_2CCH_3)_3Cl_7]^{3-}$ obtained in the X-ray structure[29] of $[NHC_5H_5]_3[Mn_4O_3Cl_7(O_2CCH_3)_3]$. [b] In angstroms. [c] In degrees.

protein conformation there is a $S = {}^3/_2$ excited state ($g = 4.1$) which is thermally populated.

Only three tetranuclear manganese complexes modeling the S_2 state have been reported: $(H_2Im)_2[Mn_4O_3Cl_6(O_2CCH_3)_3(HIm)]\cdot{}^3/_2CH_3CN$ (**2**; H_2Im^+ = imidazolium cation),[34] $[Mn_4O_3Cl_4(O_2CCH_3)_3(py)_3]\cdot{}^3/_2CH_3CN$ (**3**, py = pyridine),[35] and $[Mn_4O_3Cl(O_2CCH_3)_3(dbm)_3]$ (**4**; dbmH = dibenzoylmethane).[36] Complexes **1**–**4** have essentially superimposable distorted cubane $Mn^{IV}Mn^{III}_3O_3Cl$ cores:

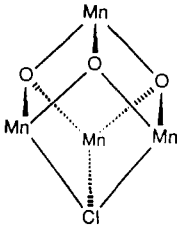

From variable-field magnetization data for complex **3** it has been established that it has a relatively isolated $S_T = {}^9/_2$ ground state.[35] Relatively weak exchange interactions are present, where for complex **3** $J_1(Mn^{IV}$–$Mn^{III}) = -26.8$ cm^{-1} and $J_2(Mn^{III}$–$Mn^{III}) = +12.1$ cm^{-1}. Since the core and susceptibility characteristics are quite similar and there are fewer atoms, $[Mn_4O_3Cl_7(O_2CCH_3)_3]^{3-}$ was selected for LCAO Xα calculations. The main parameters determining the results of the calculation are the orbital basis sets, the charge density fit sets, and the various types of exchange and correlation potentials used. All of these were used in standard form and were not altered subsequently. With no further adjustable parameters it was interesting to see if this density functional method combined with the broken symmetry methodology could calculate the correct ground-state and magnetic exchange parameters.

Experimental Section

The details of the synthesis, X-ray structure, and physical and magnetic properties of the pyridinium salt of complex **1** will be reported in a separate paper.[29] Our calculations are on the anionic Mn_4 complex and do not include the three pyridinium cations. The crystal structure of **1**, $[Mn_4O_3Cl_7(O_2CCH_3)_3]^{3-}$, did not have C_3 site symmetry. For the purposes of our calculations, the geometry of the complex was adjusted to C_{3v} symmetry. The net nuclear displacement of any atom in going from the crystal structure to C_{3v} was less than 0.01 Å. Figure 1 depicts the structure of the symmetrized complex **1**; important bond lengths and angles are given in Table I. A table of the symmetrized coordinates can be found in the supplementary material. The molecule was oriented such that the y-axis, which passes through the Mn^{IV} and μ_3-Cl atoms, coincided with the C_3 axis of the molecule and the xy plane coincided with a σ_v plane of the molecule. The calculations included 35 total atoms; there are 22 unique atoms in C_s symmetry and 11 unique atoms in C_{3v}.

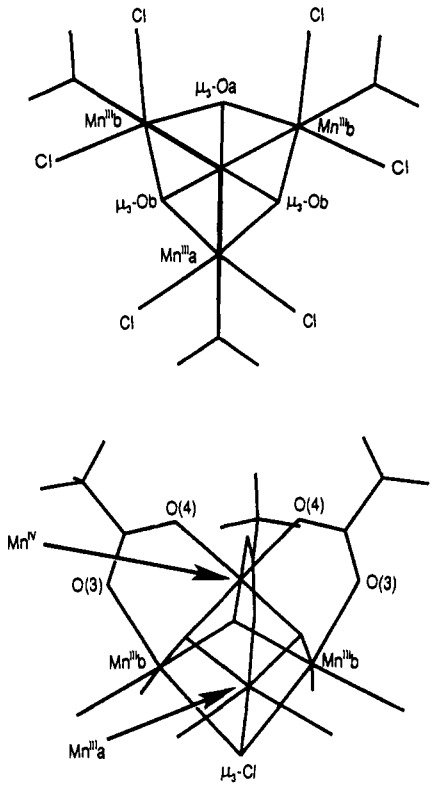

Figure 1. Structure and atom labeling scheme for $[Mn_4O_3Cl_7(O_2CCH_3)_3]^{3-}$.

All calculations were made using the Density Functional LCAO computer program of Baerends, Ros, and co-workers[37] on a Cray-XMP/SE supercomputer operated and maintained at the Scripps Research Institute, Department of Molecular Biology, La Jolla, CA. Calculations were performed using two different potentials. The potentials used were Xα ($\alpha = 0.7$)[38] and Vosko–Wilk–Nusair–Stoll LSD.[39] For a given potential, the program utilized both analytical and numerical methods to obtain solutions to the self-consistent field calculations in the LCAO form. A cellular integration method, with special rules within atomic spheres and product Gauss rules in the interstitial region, developed by Te Velde et al.[40] was used with a total nonuniform sampling of 91 804 unique points for C_s symmetry; the numerical integration accuracy parameter ACCINT was taken as 3.5. Convergence was achieved when the change in the mean of the diagonal elements of the **P** (density) matrix was less than 0.0003.

Two different Slater type basis sets with frozen cores were utilized. For Mn, the frozen core included 3s and 3p orbitals. The same Cartesian coordinate system as used to orient the molecule in space was used for the atomic orbitals which were centered at the appropriate nuclear positions. The first basis set included a triple ζ expansion of the Mn 3d orbitals and a double ζ expansion of the Mn 4s orbitals. The Cl basis set consisted of double ζ expansions for the 3s and 3p orbitals. For O

(34) Bashkin, J. S.; Chang, H.-R.; Streib, W. E.; Huffman, J. C.; Hendrickson, D. N.; Christou, G. *J. Am. Chem. Soc.* **1987**, *109*, 6502–6504.

(35) (a) Li, Q.; Vincent, J. B.; Libby, E.; Chang, H.-R.; Huffman, J. C.; Boyd, P. D. W.; Christou, G.; Hendrickson, D. N. *Angew. Chem., Int. Ed. Engl.* **1988**, *27*, 1731–1733. (b) Hendrickson, D. N.; Christou, G.; Schmitt, E. A.; Libby, E.; Bashkin, J. S.; Wang, S.; Tsai, H.-L.; Vincent, J. B.; Boyd, P. D. W.; Huffman, J. C.; Folting, K.; Li, Q.; Streib, W. E. *J. Am. Chem. Soc.* **1992**, *114*, 2455.

(36) Wang, S.; Folting, K.; Streib, W. E.; Schmitt, E. A.; McCusker, J. K.; Hendrickson, D. N.; Christou, G. *Angew. Chem., Int. Ed. Engl.* **1991**, *30*, 305–306.

(37) (a) Baerends, E. J.; Ellis, D. E.; Ros, P. *Chem. Phys.* **1973**, *2*, 41. (b) Baerends, E. J.; Ros, P. *Chem. Phys.* **1973**, *2*, 52. (c) Baerends, E. J.; Ros, P. *Chem. Phys.* **1975**, *8*, 412. (d) Bickelhaupt, F. M.; Baerends, E. J.; Ravenek, W. *Inorg. Chem.* **1990**, *29*, 350. (e) Ravenek, W. In *Scientific Computing on Supercomputers*; Devreese, J. T.; Van Camp, P. E., Eds.; Plenum: New York, 1989; pp 201–218. (f) Ziegler, T. *Chem. Rev.* **1991**, *91*, 651.

(38) (a) Slater, J. C. *Quantum Theory of Molecules and Solids*; McGraw-Hill: New York, 1974. (b) Slater, J. C. *Adv. Quantum Chem.* **1972**, *6*, 1.

(39) (a) Vosko, S. H.; Wilk, L.; Nusair, M. *Can. J. Phys.* **1980**, *58*, 1200. (b) Painter, G. S. *Phys. Rev. B* **1981**, *24*, 4264. (c) Ceperly, D. M.; Alder, B. J. *Phys. Rev. Lett.* **1980**, *45*, 566. (d) Stoll, H.; Pavlidou, C. M. E.; Preuss, H. *Theor. Chim. Acta* **1978**, *149*, 143. (e) Stoll, H.; Golka, E.; Preuss, H. *Theor. Chim. Acta* **1980**, *55*, 29.

(40) (a) Boerrigter, P. M.; te Velde, G.; Baerends, E. J. *Int. J. Quantum Chem.* **1988**, *33*, 87. (b) te Velde, G.; Baerends, E. J. *J. Comput. Chem.*, submitted for publication. (c) te Velde, G. Ph.D. Thesis, Vrije Universiteit, Amsterdam, 1990, Chapter 3, pp 142–178.

and C the basis sets comprised double ζ expansions of the respective 2s and 2p orbitals. The H basis set was formulated from a double ζ expansion of the 1s orbital. The second basis set was identical to the first with the addition of single ζ representation for Mn 4p, Cl 3d, O 3d, and H 2p orbitals. Complete details of the two basis sets including orbital exponents and corresponding information for the core and charge density fit sets can be found in the supplementary material. The total number of Cartesian/Slater type basis functions in the larger basis set B is 495.

Since these calculations required considerable computer resources and time, we summarize the requirements for these density functional LCAO calculations below. All calculations were performed on a CRAY XMP/SE supercomputer. For calculations in C_s symmetry, approximately 0.5 GB of temporary disk storage was needed, largely for the basis set numerical data, the point grid integral tape, and the fit integral tape (TAPE08, -10, -11). The numerical data for the fit functions (TAPE09) is too large to store in C_s symmetry (>2 GB) and is recomputed in each iteration. In C_{3v} symmetry, storage of all these files is feasible, and with the higher symmetry, the computation time/iteration is much shorter. It therefore makes sense to converge a calculation in C_{3v} symmetry and to use this as a starting point for subsequent C_s calculations, speeding the number of cycles to convergence of the latter. The first calculations for a given basis set and potential type were carried out for the high-spin $M_s = {}^{15}/_2$ spin alignment in C_{3v} symmetry. The first iteration typically required 10 min in C_{3v} largely to set up the temporary disk files (as above). Convergence of the C_{3v} symmetry SCF calculations is typically attained in 100–150 iterations at about 41 s/cycle. The charge density fit coefficients from $M_s = {}^{15}/_2$ were saved (TAPE13), and then the appropriate α and β coefficients were interchanged and used as starting points for the $M_s = {}^{9}/_2$ and $M_s = {}^{1}/_2$ calculations in C_s symmetry. For example, to perform the $M_s = {}^{9}/_2$ calculation, the α and β fit coefficients for the Mn^{IV} ion were interchanged. Using these coefficients as a starting point, convergence of $M_s = {}^{9}/_2, {}^{1}/_2$ was attained in 10–50 iterations in C_s symmetry. The C_s calculation required about 24 min for the first iteration and 13 min/cycle (Xα potential) or 8 min/cycle (Vosko–Wilk–Nusair potential) for subsequent iterations. Once a converged SCF solution is obtained, the programs HFS and ETS are used to evaluate the total bonding energy by an accurate energy difference method with respect to atoms or fragments. The crucial point is the use of identical grids for molecule and fragments in the energy evaluation as well as the separate and accurate calculation of the electrostatic part of the interaction energy. These methods are an improvement on the earlier Ziegler transition state method,[41] which is still utilized for purposes of energy analysis by symmetry. The program ETS is also used to give a molecular orbital Mulliken population analysis in terms of symmetrized fragment orbitals (SFOs). This requires about 25 min of CPU time.

The total bonding energy was computed by the energy difference method with respect to a reference state. In our calculations this reference state is that of the spin-restricted atoms comprising the molecule. For some calculations, a nonlocal (gradient) correction[42] to the total electron exchange energy was used. This correction, which was first proposed by Becke,[42] is treated as a perturbation energy term in this paper and affects neither the wave function nor convergence, but it does affect spin-state energies as it is dependent upon the spin alignment.

Computational Strategy. In order to assess the magnetic properties of the molecule, unrestricted density functional (DF) calculations in broken symmetry were used. Since the complete details of the broken symmetry formalism are published elsewhere,[24,27,28] we focus here mainly on aspects that are relevant to calculating the magnetic properties of anionic complex **1**. In C_{3v} symmetry the magnetic exchange interactions in complex **1** may be described by a spin Hamiltonian with two Heisenberg coupling constants: J_{34} for Mn^{III}–Mn^{IV} interactions and J_{33} for Mn^{III}–Mn^{III} interactions as in eq 1. The spins of the three Mn^{III} sites

$$\hat{H} = -2J_{33}(\hat{S}_1\cdot\hat{S}_2 + \hat{S}_1\cdot\hat{S}_3 + \hat{S}_2\cdot\hat{S}_3) - 2J_{34}(\hat{S}_1\cdot\hat{S}_4 + \hat{S}_2\cdot\hat{S}_4 + \hat{S}_3\cdot\hat{S}_4) \quad (1)$$

are $S_1 = S_2 = S_3 = 2$, and the spin of the Mn^{IV} site is $S_4 = {}^3/_2$. Application of the Kambe vector coupling method to the solution of eq 1 gives the eigenvalue expression given as eq 2,

$$E(S_T,S_A) = -J_{34}[(S_T + 1) - S_A(S_A + 1)] - J_{33}[S_A(S_A + 1)] \quad (2)$$

where $\hat{S}_A = \hat{S}_1 + \hat{S}_2 + \hat{S}_3$ and $\hat{S}_T = \hat{S}_A + \hat{S}_4$. There are 24 unique spin states as a function of $S_A = 0, ..., 6$ and $S_T = {}^1/_2, ..., {}^{15}/_2$.

In principle, J_{34} and J_{33} could be obtained directly from differences in energies for a few S_T states. The direct calculation of these pure spin states is not currently feasible within density functional theory. The calculation of broken symmetry states, however, is straightforward, and we instead employ a broken symmetry analysis to obtain J_{34} and J_{33}, which can then be used to calculate the distribution of pure spin states.

A brief summary of the basic ideas of the broken symmetry method in dinuclear and polynuclear systems follows. For detailed discussions, see refs 24, 27, and 28. The main points are the following: (a) For weakly interacting transition metal sites, each with net spin, second-order perturbation theory is adequate for the derivation of the Heisenberg spin Hamiltonian. (b) For a polynuclear complex, the Heisenberg Hamiltonian can be written as a sum of pairwise interaction terms. (c) The broken symmetry states and their energies can be related to those of pure spin eigenstates through the use of Clebsch–Gordon algebra. Specifically, the broken symmetry states are sums of outer product states in terms of monomer spins; the site spin vectors have a definite alignment, parallel or antiparallel, so M_i (the z component of spin angular momentum) is maximal for each site. For example, in a tetrameric system, the principal term is of the form $|S_1M_1\rangle|S_2M_2\rangle|S_3M_3\rangle|S_4M_4\rangle$ where $M_i = \pm S_i$. There are clearly a number of broken symmetry states depending on whether the $\pm$ sign applies for each site. For each broken symmetry state, excited configurations mix with the principal term according to second-order perturbation theory. These terms, along with direct exchange, are responsible for generating the effective spin coupling interactions. (d) Through the use of Clebsch–Gordan algebra, all terms $\langle S_i\cdot S_j\rangle$ can be evaluated for the various broken symmetry states, and each multiplied by $-2J_{ij}$. Since the different broken symmetry state energies can be directly calculated within density functional theory, this leads to a set of linear equations from which the J parameters can be determined.

The physical interactions which determine the Heisenberg spin Hamiltonian can be summarized also.[24,27,43-46] (a) Direct exchange: there is an exchange interaction between sites even without consideration of charge transfer. This interaction is ferromagnetic and ensures that for orthogonal orbitals parallel spin alignment gives the lowest energy. For nonorthogonal orbitals, or equivalently with configuration mixing, direct exchange is one term in a sum of terms of Heisenberg type (and other higher order terms in spin coupling). (b) Superexchange: mainly metal-based orbitals interact by overlap of opposite spins on neighboring centers. An alternative orthogonal orbital representation uses configuration mixing with charge-transfer excited states. The ligand part of these orbitals may also play an important role. Such interactions are antiferromagnetic and of Heisenberg type. (c) The recently rediscovered mechanism of "crossed superexchange" (originally proposed by Goodenough),[43] which is operative in high oxidation state dinuclear and polynuclear Mn complexes, is also of Heisenberg type; it is the result of an interaction between a filled orbital on one high-spin metal site with an empty metal d orbital on another site and has been shown to be ferromagnetic. (See Hotzelmann et al.)[44] (d) Ligand spin polarization: single-electron (or double-electron) excitations from doubly occupied ligand orbitals to high-spin metal sites produce a variety of coupling terms of mainly Heisenberg form, but also with smaller higher order correction terms. (e) In addition, in the presence of energetically equivalent sites of a mixed valence pair, there are additional resonance delocalization interactions (also called "double exchange") which take the form of pairwise interactions $B_{ij}(S_{ij} + {}^1/_2)$ in contrast to Heisenberg terms like $J_{ij}S_{ij}(S_{ij} + 1)$.[24d,27g-i,45,46] If, however, the sites are energetically inequivalent due to differences in coordination geometry, these resonance terms can be quenched. (The tetranuclear Mn cluster in the present work has different coordination environments for Mn^{III} and Mn^{IV} based on our calculations; see below. The environments are sufficiently different to quench any resonance terms. These may then be absorbed into the Heisenberg J parameters.[46])

A broken symmetry state differs from a pure spin state in that it comprises a linear combination of pure states. Fortunately, the precise composition of a broken symmetry state can be computed, and more importantly, J values can be determined from differences in the energies of broken symmetry states. Conceptually, a broken symmetry state may be thought of as follows. Recognizing that each transition metal ion has a net spin ($S = 2$ for Mn^{III} and $S = {}^3/_2$ for Mn^{IV}), one may construct broken symmetry states by aligning the net spin density at each ion either up (α) or down (β). For complex **1**, we consider the three broken symmetry states where $M_s = {}^{15}/_2$, $M_s = {}^{9}/_2$, and $M_s = {}^{1}/_2$. A pictorial

(41) Ziegler, T.; Rauk, A. *Theor. Chim. Acta* **1977**, *46*, 1.

(42) (a) Becke, A. D. *J. Chem. Phys.* **1986**, *84*, 4524. (b) Becke, A. D. In *The Challenge of d and f Electrons*; Salahub, D. R., Zerner, M. C., Eds.; ACS Symp. Series 394; American Chemical Society: Washington, DC, 1989; p 165.

(43) (a) Goodenough, J. B. *Magnetism and the Chemical Bond*; Interscience Publishers: New York, 1963. (b) Ginsberg, A. P. *Inorg. Chim. Acta* **1971**, 45.

(44) Hotzelmann, R.; Wieghardt, K.; Florke, U.; Haupt, H.-J.; Weatherburn, D. C.; Bonvoision, J.; Blondin, G.; Girerd, J.-J. *J. Am. Chem. Soc.* **1992**, *114*, 1681.

(45) Anderson, P. W.; Hasegawa, H. *Phys. Rev.* **1955**, *100*, 675.

(46) Blondin, G.; Girerd, J.-J. *Chem. Rev.* **1990**, *90*, 1359.

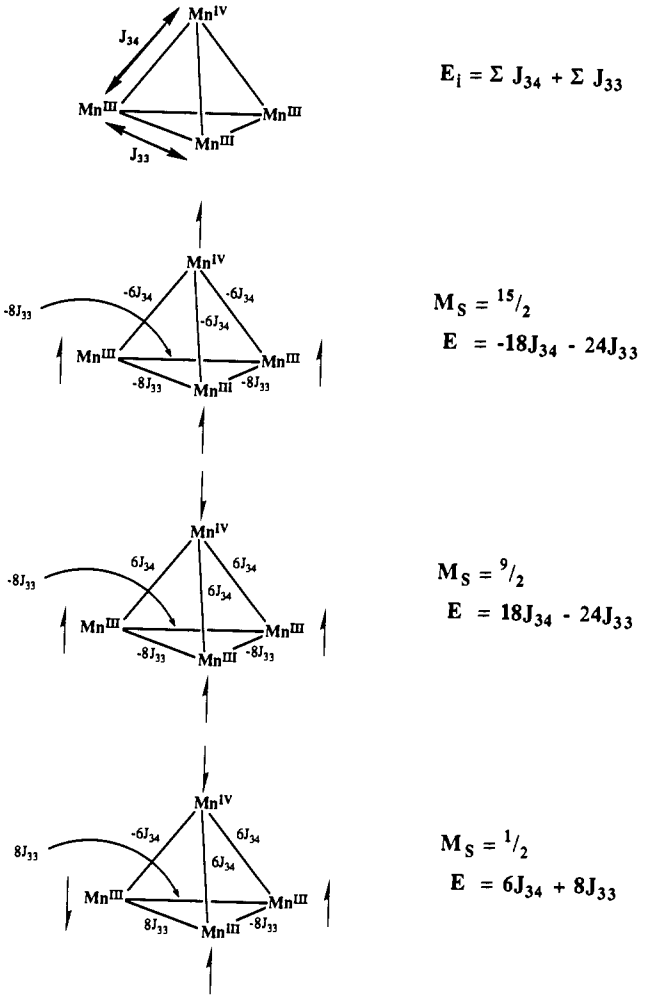

Figure 2. Diagramatic representation and energy expressions for the broken symmetry states $M_s = {}^{15}/_2$, ${}^{9}/_2$, and ${}^{1}/_2$ of a $Mn^{III}_3Mn^{IV}$ cubane complex. In the diagram for each broken symmetry state (i.e., single determinantal wavefunction) the pairwise magnetic exchange interactions are indicated in terms of the exchange parameters J_{34} and J_{33}.

representation of these broken symmetry states as well as the exchange model is given in Figure 2. The maximum spin possible for a $Mn^{III}_3Mn^{IV}$ complex is $S = {}^{15}/_2$, and the $M_s = {}^{15}/_2$ broken symmetry state in Figure 2 closely resembles this state. Flipping the Mn^{IV} spin of the $M_s = {}^{15}/_2$ state such that it is oppositely aligned with the other three Mn^{III} spins gives the $M_s = {}^{9}/_2$ broken symmetry state. While this broken symmetry state resembles the $S_T = {}^{9}/_2$, $S_A = 6$ spin state, it also contains an admixture of other spin states having $S_T \geq {}^{9}/_2$. In a similar fashion, flipping a Mn^{III} spin in going from $M_s = {}^{9}/_2$ to $M_s = {}^{1}/_2$ gives a $M_s = {}^{1}/_2$ broken symmetry state that is a mixture of $S_T \geq {}^{1}/_2$ spin states. While the molecule has C_{3v} nuclear symmetry and the $M_s = {}^{15}/_2$ and $M_s = {}^{9}/_2$ broken symmetry states preserve this, the symmetry of the spins in the $M_s = {}^{1}/_2$ broken symmetry state is C_s. Because of this, and the advantages of preserving the same numerical sampling for the different calculations, all calculations reported were done in C_s symmetry. Some initial calculations in C_{3v} symmetry yielded essentially the same energy as in the C_s symmetry. The energies of the broken symmetry states are given by eq 3:

$$\hat{H} = \Sigma -2J_{ij}\langle \hat{S}_i \hat{S}_j \rangle \tag{3}$$

where for $S_i = {}^{3}/_2$, $S_j = 2$, eq 3 gives $-2J_{ij}\langle S_i S_j \rangle = \pm 6J_{34}$ and for $S_i = S_j = 2$, eq 3 gives $-2J_{ij}\langle S_i S_j \rangle = \pm 8J_{33}$ where plus (minus) is for antiparallel (parallel) alignment of spins. The energies of the $M_s = {}^{15}/_2$, $M_s = {}^{9}/_2$, and $M_s = {}^{1}/_2$ states are given in Table II; see Figure 2 for the equations relating these energies to the magnetic exchange parameters J_{33} and J_{34}. We are not, however, concerned with the absolute energies of each broken symmetry state, but instead the relative energies. If we choose $M_s = {}^{9}/_2$ as a reference state, it is intuitive that the relative energy of the $M_s = {}^{15}/_2$ broken symmetry state is closely related to J_{34}. The same is true for the $M_s = {}^{1}/_2$ state and J_{33}, although the relationship is less straightforward. The values of J_{34} and J_{33} may be calculated from the relative energies of these three broken symmetry states as given by

Table II. Calculated Bonding Energies and Heisenberg Coupling Constants for $[Mn_4O_3(O_2CCH_3)_3Cl_7]^{3-}$ (**1**)

description	bonding energy (eV)	J_{34} (cm^{-1})	J_{33} (cm^{-1})
Xα, basis set A		−59.1	25.7
$M_s = {}^{15}/_2$	−208.546		
$M_s = {}^{9}/_2$	−208.810		
$M_s = {}^{1}/_2$	−208.620		
Xα, basis set B		−54.0	28.1
$M_s = {}^{15}/_2$	−216.853		
$M_s = {}^{9}/_2$	−217.094		
$M_s = {}^{1}/_2$	−216.902		
Xα, basis set B, Becke		−46.6	19.3
$M_s = {}^{15}/_2$	−182.974		
$M_s = {}^{9}/_2$	−183.182		
$M_s = {}^{1}/_2$	−183.036		
VWNS, basis set B		−94.1	19.4
$M_s = {}^{15}/_2$	−213.337		
$M_s = {}^{9}/_2$	−213.757		
$M_s = {}^{1}/_2$	−213.540		
VWNS, basis set B, Becke		−79.5	12.8
$M_s = {}^{15}/_2$	−178.879		
$M_s = {}^{9}/_2$	−179.234		
$M_s = {}^{1}/_2$	−179.065		

eqs 4 and 5, which follow directly by simple algebra from the broken symmetry state energies given in Figure 2. Once J_{34} and J_{33} have been

$$J_{34} = -(E_{15/2} - E_{9/2})/36 \tag{4}$$

$$J_{33} = (E_{1/2} - E_{9/2} + 12J_{34})/32 \tag{5}$$

determined, the energies of the pure spin states are easily determined by using eq 2.

A few additional comments on the broken symmetry state energies are in order. We note that changing the sign of M_s has no effect on either the state energy or the orbital part of any broken symmetry wave function but only interchanges the α and β spin functions. Of more physical significance, it is also possible to calculate the broken symmetry state $M_s = {}^{7}/_2$ obtained by aligning two of the Mn^{III} sites with the Mn^{IV} and oppositely aligning these with the third Mn^{III} site. This is not necessary since $M_s = {}^{15}/_2$, ${}^{9}/_2$, and ${}^{1}/_2$ are sufficient to uniquely determine J_{33} and J_{34}. It would be useful, however, to have a set of overdetermined equations to further establish the internal consistency of the theoretical methodology. This calculation will be pursued in future work.

Results and Discussion

Bonding Energies of Broken Symmetry States. The bonding energies calculated for the experimentally known complex **1**, $[Mn_4O_3Cl_7(O_2CCH_3)_3]^{3-}$, are listed in Table II. The bonding energies listed are with respect to the spin-restricted atoms as computed by the energy difference method. It can be seen that in going from one potential to another the computed bonding energies vary widely from a minimum of −217.094 eV to a maximum of −178.879 eV. This is a reflection of the different potentials and basis sets used. It should also be noted that the variational minimum energy principle does not apply when comparing one density functional potential to the next. (However, the variational principle does apply when comparing basis sets (A and B) within a single type of potential.) The effect of the Becke energy term is to substantially raise the bonding energy (weaker bonding). In previous problems this has been found to improve calculated bond energies compared to experiment. Further, in order to obtain the true "bonding energy" the physical molecular bonding energy should be defined with respect to spin-polarized atom fragments with the same potential and energy correction terms. This is not pursued here. Rather, the range of calculated bond energies is not of direct concern since we are interested in the relative bond energies for the spin-coupling problem. For any given potential and basis set, the variation in bond energies over M_s values is small. More importantly the energetic ordering of broken symmetry states consistently gives $M_s = {}^{9}/_2$ as the ground state followed by $M_s = {}^{1}/_2$ and $M_s = {}^{15}/_2$ broken symmetry states. From these separations in energies, the values of J_{34} and J_{33} were computed using eqs 4 and 5. The values of J_{34} and J_{33} for each set of broken symmetry calculations are

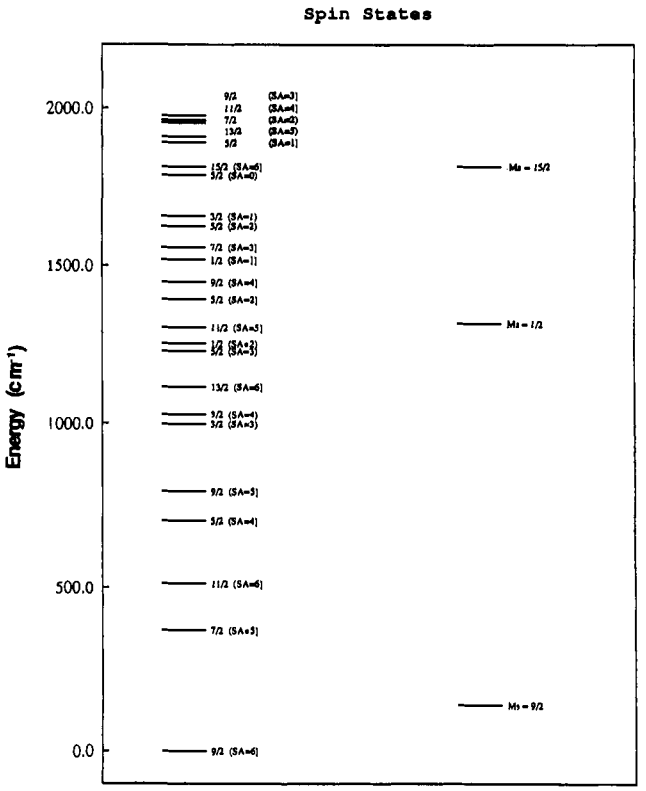

Figure 3. Calculated energies for the $M_s = {}^{15}/_2$, ${}^{9}/_2$, and ${}^{1}/_2$ broken symmetry states (right) and all pure spin states (left) for $[Mn_4O_3Cl_7(O_2CCH_3)_3]^{3-}$.

listed in Table II. In each case, J_{34} is antiferromagnetic and J_{33} is ferromagnetic, ranging from −94.1 to −46.6 cm^{-1} and 12.8 to 28.1 cm^{-1}, respectively. By substituting these J values into eq 2, the energies of the pure spin states may be computed. Figure 3 shows the spin-state ladder calculated for $J_{34} = -46.6$ cm^{-1} and $J_{33} = 19.3$ cm^{-1}. It is clear that these LCAO Xα calculations give a $S_T = {}^{9}/_2$ ground state in agreement with experimental susceptibility results.[35] The energy levels plotted in Figure 3 are relative energies with the $M_s = {}^{15}/_2$ broken symmetry state closely resembling the $S = {}^{15}/_2$ state. Substitution of the energies for the pure spin states into the Van Vleck equation gives an expression for the temperature-dependent susceptibility.

Magnetochemistry. Theoretical magnetic moment versus temperature curves were computed for each set of J values given in Table II. Figure 4 shows a plot of experimental and theoretical magnetic moments versus temperature for the pyridinium salt of complex **1**. The values of J_{34} and J_{33} used to calculate the theoretical curve were those obtained from calculations employing the Xα potential, larger basis set (B), and Becke correction and gave the best agreement with experimental results. The value of $g = 2.02$ used was chosen to optimize agreement between experimental and theoretical moments and is in close agreement with the g values reported[33,34] for complexes **2** and **3**. It is important to emphasize that the theoretical curve in Figure 4 is not the result of fitting the data to a model, but is instead computed directly from the J values obtained by our calculations. While the theoretical curve misses the experimental data at low temperature, this is very likely a reflection of zero field splitting of the $S = {}^{9}/_2$ ground state and is a feature not included in the Van Vleck equation in this case. In general, results obtained using the Xα potential are superior to those obtained using the LSD potentials. It should be noted that flipping a spin affects only a ~0.1% difference in the bonding energy and that calculated J values are 4–5 orders of magnitude smaller than the calculated bonding energies. With this in mind, all of the calculations are quite good. We found the excellent agreement between experimental and calculated magnetic moments to be beyond our expectations given that the spin-coupling energies are about ${}^{1}/_3$–${}^{1}/_{10}$ those found in Fe–S complexes. The remainder of this paper will focus on the

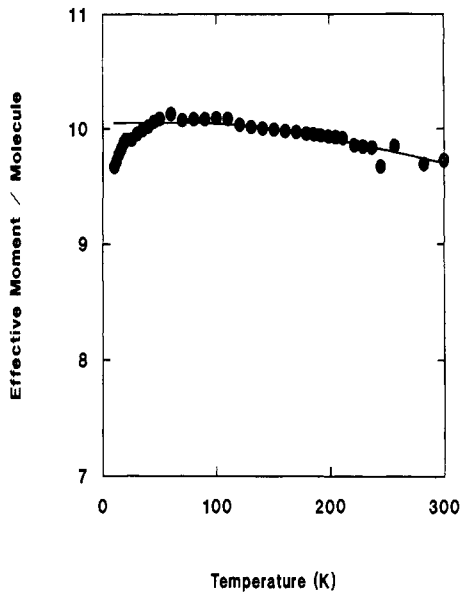

Figure 4. Plot of experimental (circles) and theoretical (solid line) effective magnetic moments/molecule versus temperature for $[HNC_5H_5]_3[Mn_4O_3Cl_7(O_2CCH_3)_3]$. Theoretical moments were calculated from the HDVV model using values of $J_{33} = +19.3$ cm^{-1} and $J_{34} = -46.6$ cm^{-1} obtained from the broken symmetry analysis of the Xα calculations using the second (larger) basis set and the Becke correction. A value of $g = 2.02$ was chosen to give the best agreement between experimental and theoretical data sets.

Table III. Composition of the Frontier Orbitals Calculated for the $M_s = {}^{9}/_2$ Broken Symmetry State[a]

molecular orbital	energy (eV)	description
A′-α (50)		
NHOMO	4.402	Mn^{III}_b d_{yz} (16.0); μ_3-Cl p_y (19.9)
HOMO	4.466	Mn^{III}_a d_{xy} (21.1); μ_3-Cl p_x (21.1)
LUMO	5.447	Mn^{III}_b d_{z^2} (20.9); t-Cl p_x (11.1)
NLUMO	5.889	Mn^{IV} d_{z^2} (35.1), $d_{x^2-y^2}$ (13.1), d_{xy} (20.6)
A″-α (38)		
NHOMO	3.854	t-Cl p_x (43.5), p_z (44.3)
HOMO	4.464	Mn^{III}_b $d_{x^2-y^2}$ (10.2), d_{xy} (22.5); μ_3-Cl p_z (21.2)
LUMO	5.445	Mn^{III}_a d_{xz} (20.2); t-Cl p_z (11.3); μ_3-O p_y (11.7)
NLUMO	5.897	Mn^{IV} d_{xz} (48.5), d_{yz} (20.7)
A′-β (45)		
NHOMO	3.358	Mn^{IV} $d_{x^2-y^2}$ (27.2); μ_3-Cl p_y (19.1); μ_3-O p_y (12.1)
HOMO	3.518	t-Cl p_x (46.8), p_z (15.7)
LUMO	5.843	Mn^{IV} d_{xy} (26.7)
NLUMO	6.630	Mn^{III}_a $d_{x^2-y^2}$ (24.7); Mn^{III}_b d_{xy} (23.5), d_{yz} (18.2)
A″-β (34)		
NHOMO	3.517	t-Cl p_x (13.8), p_z (60.0)
HOMO	3.851	t-Cl p_x (42.8), p_z (46.0)
LUMO	5.846	Mn^{IV} d_{xz} (10.5), d_{yz} (26.6)
NLUMO	6.628	Mn^{III}_a d_{yz} (29.3); Mn^{III}_b d_{z^2} (11.1), d_{xy} (17.6), $d_{x^2-y^2}$ (15.0)

[a] HOMO is the highest energy occupied MO; LUMO is the lowest energy unoccupied MO; NHOMO (NLUMO) is the next highest (lowest) energy MO.

analysis of those results obtained using the Xα potential, larger basis set, and Becke correction. Similar results were obtained for the other potentials and basis sets.

Molecular Orbital Analysis. Since the calculations on $[Mn_4O_3(O_2CCH_3)_3Cl_7]^{3-}$, complex **1**, were done in C_s symmetry, the molecular orbitals have either A′ or A″ symmetry. For **1** there are 167 occupied molecular orbitals. Descriptions of the highest occupied MO (HOMO), next HOMO (NHOMO), lowest unoccupied MO (LUMO), and next LUMO (NLUMO) for each representation and spin index in the $M_s = {}^{9}/_2$ broken symmetry state are given in Table III, and complete descriptions of all of

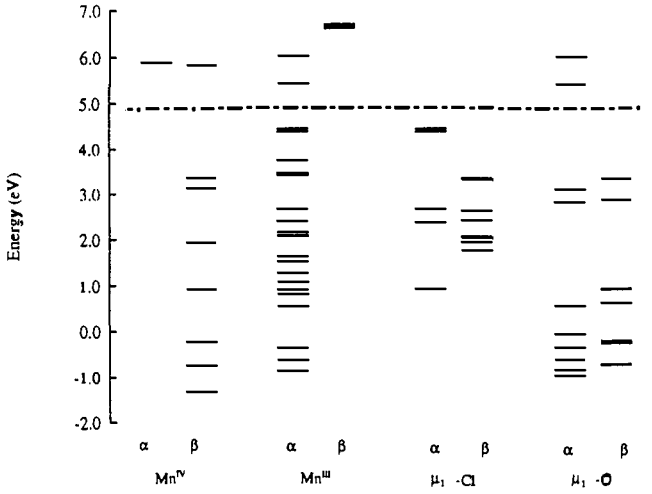

Figure 5. Plot of the molecular orbital energy levels for the $M_s = {}^9/_2$ broken symmetry state. The orbitals are sorted according to spin (α or β) and atom type contributing to the orbital.

the occupied (and some unoccupied) orbitals for each broken symmetry state are given in the supplementary material. There are several features of this analysis which warrant discussion. First, most of the molecular orbitals show extensive mixing of atomic orbitals. For example, if we consider the A'-α HOMO of the $M_s = {}^9/_2$ state as given in Table III, this orbital is delocalized such that 21.1% of the α electron density resides in the $Mn^{III}{}_a d_{xy}$ orbital and 21.1% resides in the μ_3-Cl p_x orbital. The remaining 57.8% of the electron density is delocalized throughout the molecule such that no more than 10% can be found in any atomic orbital. This extent of delocalization is typical for all of the occupied molecular orbitals. One reason for such extensive mixing of atomic orbitals is the presence of covalency in the bonding, but this mixing is also a consequence of several other factors. These factors include the symmetry used (C_s) and the orientation of the atomic basis functions. For instance, inspection of the structure shows that the μ_3-Cl-Mn^{III}-O(acetate) axis is the axis of Jahn-Teller distortion and the "local" Mn^{III} z-axis. The z-axes as defined for the Mn^{III} basis functions in the calculation, however, are parallel to the global z-axis of the cluster (similarly for x, y; see Table SI); the global z-axis is perpendicular to the plane defined by Mn^{IV}-$Mn^{III}{}_a$-μ_3-Cl for the C_s symmetry. Therefore, orbitals which lie along the "local" Mn^{III} z-axis such as d_{z^2} become an appropriate linear combination of atomic basis functions in the context of the calculations.

The energies of the HOMOs and several of the other occupied MOs are positive. This is a consequence of complex **1** being an anion with a 3- charge. In solution and in the solid state this charge would be stabilized by the pyridinium cations and by solvation.

An energy level diagram depicting those MOs containing significant Mn d-orbital character and/or significant μ_3-Cl or μ_3-O p-orbital character for the $M_s = {}^9/_2$ broken symmetry state is given in Figure 5. These energy levels are sorted according to spin and major contributor (>10%). The distribution of MO energy levels containing considerable Mn ion character is consistent with the $M_s = {}^9/_2$ broken symmetry state where the net spin is β at the Mn^{IV} site and α at the Mn^{III} sites and with the ideas of extensive mixing discussed above. Similar MO diagrams for the $M_s = {}^{15}/_2$ and $M_s = {}^1/_2$ broken symmetry states track the Mn net spin densities equally well. Another observation is that the distribution of occupied MOs containing Mn^{IV} character is slightly lower in energy than the corresponding distribution containing Mn^{III} character. Finally, ligand orbitals are distributed throughout both α and β spin MOs, and in general the distributions of MOs containing μ_3-O character are lower in energy than those containing μ_3-Cl.

Population Analysis. Table IV lists the charges and net spin of several atoms comprising **1** for each of the three broken symmetry states. These values were obtained directly from a Mulliken type population analysis. Net spin is simply the difference between α and β spin densities at an atom such that a negative net spin density implies a net β spin at that atom. Atom labels were chosen such that an "a" type atom is a unique atom lying on the mirror plane in C_s symmetry, and "b" type atoms are reflected through the mirror plane, as indicated in Figure 1.

Table IV. Charges and Net Spin Densities Calculated for the Broken Symmetry States of Selected Atoms of $[Mn_4O_3(O_2CCH_3)_3Cl_7]^{3-}$

	$M_s = {}^{15}/_2$		$M_s = {}^9/_2$		$M_s = {}^1/_2$	
	charge	net spin	charge	net spin	charge	net spin
$Mn^{III}{}_a$	0.760	3.894	0.758	3.880	0.758	-3.881
$Mn^{III}{}_b$	0.761	3.894	0.759	3.881	0.759	3.870
Mn^{IV}	1.138	2.915	1.111	-2.734	1.117	-2.783
μ_3-Cl	-0.370	0.186	-0.354	0.134	-0.369	0.023
μ_3-O_a	-0.695	-0.031	-0.686	-0.112	-0.685	-0.117
μ_3-O_b	-0.695	-0.031	-0.686	-0.112	-0.692	-0.040
$O(3)_a$	-0.837	0.052	-0.841	0.023	-0.839	-0.056
$O(3)_b$	-0.842	0.052	-0.846	0.022	-0.844	0.025
$O(4)_a$	-0.840	0.010	-0.839	0.011	-0.838	-0.001
$O(4)_b$	-0.835	0.008	-0.834	0.012	-0.834	0.008
Cl_a	-0.443	0.018	-0.442	0.029	-0.438	-0.002
Cl_b	-0.442	0.018	-0.441	0.029	-0.438	0.018
Cl_b	-0.442	0.018	-0.442	0.029	-0.440	0.026

Only very small changes in atomic charges are found for the different broken symmetry states. There are, however, several interesting features in the overall charge distribution. While the Mn atoms are assigned formal oxidation states of +3 or +4, their calculated charges are much smaller; for $M_s = {}^9/_2$ these are +0.76 and +1.11, respectively. Significantly distinct Mn^{III} and Mn^{IV} ions are found as opposed to complete delocalization. This result is consistent with the different coordination environments of the Mn^{III} and Mn^{IV} ions. The Mn^{III} ion has longer Mn-μ_3-O bond distances and a Jahn-Teller distortion along the μ_3-Cl-Mn^{III}-O-(acetate) axis that is characteristic of a d^4 Mn^{III} ion. The μ_3-O and Cl atoms, which formally have 2- and 1- charges, respectively, also have smaller calculated charges. These results suggest that there is appreciable covalency in the bonding.

The net spin densities are informative. The Mn^{III} and Mn^{IV} ions are expected to have four and three unpaired electrons, respectively. The net spin densities of the Mn ions are quite close to this, and their change in sign closely follows the flipping of spins necessary in going from one broken symmetry state to another. The net spin densities of the ligands vary considerably with each broken symmetry state. The largest net spin density found on any ligand is on the μ_3-Cl atom that bridges only the three Mn^{III} ions. The net spin density on this μ_3-Cl atom varies from 0.186 to 0.134 to 0.023 upon going from the $M_s = {}^{15}/_2$ to ${}^9/_2$ to ${}^1/_2$ state. The large change in net spin density upon going from the $M_s = {}^{15}/_2$ state to the $M_s = {}^9/_2$ state was unexpected considering that it is the Mn^{IV} spin that is flipped and the μ_3-Cl bridges the three Mn^{III} ions. The net spin densities of the three μ_3-O atoms also vary considerably with broken symmetry. Each μ_3-O bridges two Mn^{III} ions and the Mn^{IV} ion. Over the three broken symmetry states examined, the three μ_3-O atoms can be found to be in essentially three different environments, as depicted in Figure 6. The largest net spin on a μ_3-O atom occurs for case B when the Mn^{IV} is β and the two coordinated Mn^{III} ions are α as in $M_s = {}^9/_2$ and μ_3-O_a of the $M_s = {}^1/_2$ broken symmetry state. The smallest net spin is for case A when all spins are aligned. This trend closely follows the energetic ordering of the three broken symmetry states, i.e., the largest μ_3-O net spin density gives the most stable state, whereas the smallest μ_3-O net spin density leads to the least stable state.

Spin Donors and Ligand Spin Polarization. From the calculated charges, it is apparent that the ligands are donating considerable electron density to the Mn ions. The net spin densities show that there is in some cases a propensity to donate more of one spin (α or β) than the other. In the case of the μ_3-Cl atom the net spin density of the Cl atom is α for all three broken symmetry states. If one starts with a diamagnetic Cl^- ion, and then through in-

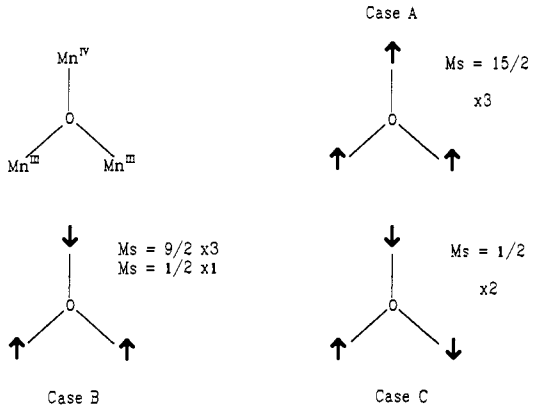

Figure 6. Pictorial representation of the three possible spin environments for a μ_3-O atom in $[Mn_4O_3Cl_7(O_2CCH_3)_3]^{3-}$. Each case is labeled with the broken symmetry state it occurs in and the number of instances ($\times N$) for that state.

teractions with the three Mn^{III} ions a Cl atom having a net α spin density is produced, it may be concluded that the Cl is a net β spin donor. While the μ_3-Cl atom is a net β spin donor, it is important to note that the μ_3-Cl atom donates both α and β spin density to the Mn^{III} ions. For instance, in the $M_s = {}^9/_2$ broken symmetry state the μ_3-Cl atom donates 0.256 e^- of α type spin density and 0.390 e^- of β spin density, which results in 3.744 α and 3.610 β type spin density. The three μ_3-O atoms have a net β spin density and are therefore net α donors.

The net spin density of complex **1** was calculated over a uniformly spaced three-dimensional grid of 32 768 points (32 × 32 × 32) confined within a cube 15 bohr to a side using the program EO developed by M. Pique of The Scripps Research Institute. This program was adapted for use with Silicon Graphics Iris contouring software from the San Diego Supercomputer Center. It is possible to examine the distribution of net spin density throughout the molecule by taking slices through this grid. The nature of spin donation is revealed by taking slices perpendicular to the C_3 axis and midway between the Mn^{IV}–μ_3-O's and Mn^{III}–μ_3-O's. Figures 7–9 show iso net spin density contours of these slices for each of the broken symmetry states, $M_s = {}^9/_2$, ${}^1/_2$, and ${}^{15}/_2$, respectively. The solid lines in Figures 7–9 depict regions with α net spin densities, and the dashed lines represent regions of β net spin density. The three μ_3-O atoms show evidence of spin polarization, which is particularly evident in the $M_s = {}^9/_2$ and $M_s = {}^1/_2$ broken symmetry states. For the $M_s = {}^9/_2$ state the Mn^{IV} ion is predominantly β spin, with the three μ_3-O atoms having net α spin pointing toward the Mn^{IV} ion and net β spin away. Following the convention for spin donation described above, the three μ_3-O atoms are net β spin donors to the Mn^{IV} ion, and with respect to the Mn^{III} ions, they are net α spin donors. For the $M_s = {}^1/_2$ broken symmetry state, one Mn^{III} spin has been flipped. Spin polarizations of all three μ_3-O atoms relative to the Mn^{IV} ion are essentially identical to that found in the $M_s = {}^9/_2$ broken symmetry state. The flipped (β) Mn^{III} spin does, however, have a dramatic effect on the two μ_3-O atoms bonded to it. These two μ_3-O atoms are net β spin donors to the β spin Mn^{III} and net α spin donors to the two α spin Mn^{III} ions. The net spin density contour diagrams for the $M_s = {}^{15}/_2$ broken symmetry state shown in Figure 9 do not show appreciable μ_3-O spin polarization. In fact, since the net spin densities on the μ_3-O atoms are so small, the contours are relatively featureless. A similar type of analysis for the Mn^{III}–μ_3-Cl interaction reveals that the μ_3-Cl atom always has net α spin density directed along the C_3 axis which passes through it.

Magnetic Exchange Interaction Mechanism and Pathways. Figure 5 ($M_s = {}^9/_2$) shows that the high-spin Mn ions in this complex display an "inverted level" scheme in bonding. This applies to all the different M_s spin alignments examined. For the $M_s = {}^9/_2$ broken symmetry state, levels with substantial (≥10%) majority spin Mn^{IV} β spin character and those with substantial Mn^{III} α spin character are strongly stabilized by Mn intraatomic

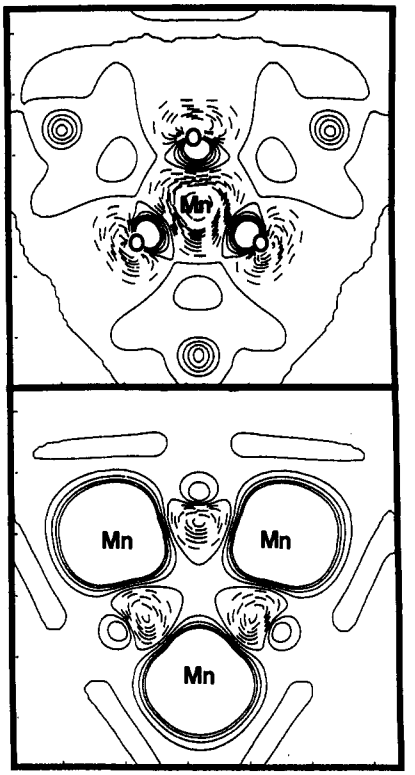

Figure 7. Contour plot showing the net spin density for the $M_s = {}^9/_2$ broken symmetry state of $[Mn_4O_3Cl_7(O_2CCH_3)_3]^{3-}$. The planes represented by the contour plots are perpendicular to the C_3 axis midway between the Mn^{IV} and three μ_3-O atoms for the top plot; midway between the Mn^{III} and three μ_3-O atoms for the bottom plot. Net α spin density is represented by the solid lines, and net β spin density is represented by the dashed lines.

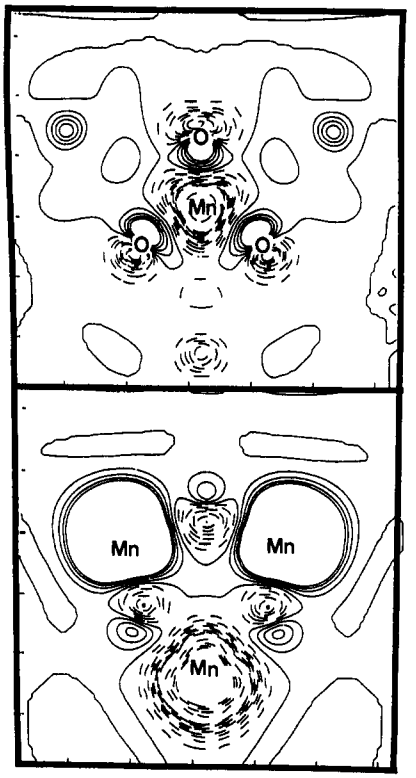

Figure 8. Contour plot showing the net spin density for the $M_s = {}^1/_2$ broken symmetry state of $[Mn_4O_3Cl_7(O_2CCH_3)_3]^{3-}$. The planes represented by the contour plots are perpendicular to the C_3 axis midway between the Mn^{IV} and three μ_3-O atoms for the top plot; midway between the Mn^{III} and three μ_3-O atoms for the bottom plot. Net α spin density is represented by the solid lines, and net β spin density is represented by the dashed lines.

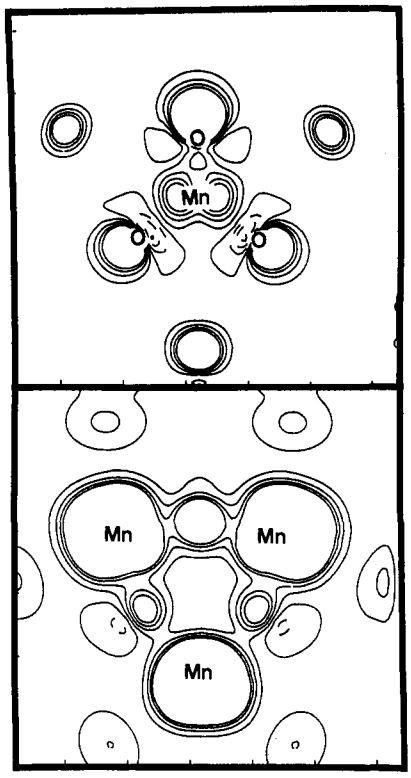

Figure 9. Contour plot showing the net spin density for the $M_s = {}^{15}/_2$ broken symmetry state of $[Mn_4O_3Cl_7(O_2CCH_3)_3]^{3-}$. The planes represented by the contour plots are perpendicular to the C_3 axis midway between the Mn^{IV} and three μ_3-O atoms for the top plot; midway between the Mn^{III} and three μ_3-O atoms for the bottom plot. Net α spin density is represented by the solid lines, and net β spin density is represented by the dashed lines.

exchange (equivalently, by strong spin polarization on the metal sites), while the corresponding levels with substantial Mn minority spin character are destabilized and appear above the Fermi level. The occupied ligand levels are interspersed with and heavily mixed with the majority spin Mn levels. In the occupied orbitals, total Mn character is usually less than 40% (10–30% is typical), so that it becomes impossible to identify a small set of "magnetic orbitals" with strong metal character which are responsible for the spin coupling. This is quite different from Cu^{II}–Cu^{II} (d^9–d^9) complexes,[8-12,18-22] and also unlike dinuclear and polynuclear Fe_nS_m clusters.[4,5,27] In both of these, superexchange is considered as a strong contributor to spin coupling. Further evidence for the importance of superexchange in dinuclear and polynuclear FeS clusters is that the net spin populations on the metals drop significantly (typically by 0.3–0.5 e^- for $Fe_4S_4^{2+,1+}$) when there is antiparallel alignment of spin vectors, compared to parallel alignment.[27] By contrast, there is a change of only +0.18 e^- in the magnitude of the Mn^{IV} spin population on going from $M_s = {}^{15}/_2$ to $M_s = {}^9/_2$, and only +0.05 from $M_s = {}^9/_2$ to $M_s = {}^1/_2$. The magnitude of the $Mn^{III}_{a,b}$ spin populations is nearly invariant with spin alignment.

The behavior of the spin coupling with respect to the metal coordination geometry is also surprising. Conventional thinking would suggest that the 116° Mn^{III}–μ_3-O–Mn^{III} bond angle would lead to a more antiferromagnetic Mn^{III}–Mn^{III} than Mn^{III}–Mn^{IV} interaction, since the latter has a 95° Mn^{III}–μ_3-O–Mn^{IV} bond angle. In fact, just the opposite trend is found both theoretically and experimentally as inferred from the magnetic susceptibility versus temperature data. We consider then that spin polarization of the bridging and terminal ligands is the major contributor to spin coupling. This contribution may arise either from a lowering of the ligand electron exchange energy or through enhanced $L \rightarrow M$ transfer terms with spin polarization of the ligands.

In the preceding section, we introduced trends in spin donation by μ_3-Cl and μ_3-O based on spin density maps and Mulliken spin populations on the ligands for different spin states. Now we analyze the complexity of the spin-transfer pathways in the Mn_4O_3Cl cubane system. We refine our previous concept of α and β spin donors by introducing the idea of "majority" and "minority" spin donors. Consider initially the μ_3-O anions and the $M_s = {}^9/_2$ broken symmetry state. In Figure 7 (bottom), the μ_3-O sites have net β spin adjacent to the α spin Mn^{III} sites; α spin is then considered to be donated to the adjacent Mn^{III} sites, and the μ_3-O atoms are majority spin donors to the Mn^{III} ions. Figure 7 (top) shows that immediately adjacent to the Mn^{IV} spin β site the μ_3-O spin density is α; β spin is donated so that the μ_3-O atoms are also majority spin donors to Mn^{IV}. The $M_s = {}^9/_2$ and ${}^1/_2$ spin alignments depicted in Figures 6–8 show the μ_3-O atoms as majority spin donors to all Mn^{III} and Mn^{IV}. This is further supported by the Mulliken spin populations in Table IV. By plotting the two parallel slices in three dimensions, it was noted that the regions of excess α and β spin density on a μ_3-O atom arise from p-orbitals of different, but not necessarily orthogonal, orientation. The $M_s = {}^{15}/_2$ spin density shown in Figure 9 is more ambiguous about the sign of the net spin donation from $L \rightarrow M$; here the Mulliken spin populations indicate the μ_3-O to be a majority spin donor in the $M_s = {}^{15}/_2$ state although a weak one.

By similar analysis, it was found that the μ_3-Cl atom is a minority spin donor. Further, by summing the spin density populations (Table IV) over all the terminal Cl atoms and carboxylate O atoms, we conclude that together these act as minority spin donors. Quantitatively, the total terminal ligand spin populations over all Cl_t and terminal O atoms are +0.290, +0.276, and +0.093 (net α) for $M_s = {}^{15}/_2$, ${}^9/_2$, and ${}^1/_2$, respectively. Similarly, the μ_3-Cl atom spin populations are +0.186, +0.134, and +0.023. By contrast, the μ_3-O atom spin populations/atom are –0.031, –0.112, and (–0.117 μ_3-O_a–0.040 μ_3-O_b) for $M_s = {}^{15}/_2$, ${}^9/_2$, and ${}^1/_2$.

The calculations have established $M_s = {}^9/_2$ as the lowest broken symmetry state, followed by $M_s = {}^1/_2$ and $M_s = {}^{15}/_2$, respectively. Correspondingly, J_{34} was found to be antiferromagnetic and J_{33} ferromagnetic with $|J_{34}|$ two or more times $|J_{33}|$ in magnitude. The parameter J_{34} is completely determined by the energy difference between the $M_s = {}^{15}/_2$ and $M_s = {}^9/_2$ broken symmetry states. As previously mentioned, the largest μ_3-O atom spin population is associated with the lowest energy broken symmetry state, and in fact, the energetic ordering of each broken symmetry state follows the magnitude of the corresponding μ_3-O atom spin population. Majority spin donation by the μ_3-O sites then plays the most important role in stabilizing the $M_s = {}^9/_2$ broken symmetry state. Both majority spin and minority spin donation from different ligands can exist in systems like this Mn_4 cubane where the Mn^{III},Mn^{IV} oxidation states are formally associated with less than a half-filled d shell (formally d^4, d^3). Even after electron transfer and spin transfer from the ligands, the Mn sites have fewer than five majority spin d electrons. For example, with $M_s = {}^9/_2$, the Mn ($3d\alpha$, $3d\beta$) populations are (4.57, 0.82) on Mn^{III} and (1.30, 3.98) on Mn^{IV}. By contrast, $Cu(d^9)$[8-12] and $Fe(d^{5,6})$[27] systems each have greater than or equal to a half-filled shell both formally and according to Mulliken analyses. In these cases, the ligand spin donation is always of minority spin by the Pauli exclusion principle.

But even with the possibility of both majority spin and minority spin donation from different ligands, why do the μ_3-O atoms serve as majority spin donors and the μ_3-Cl as a minority spin donor? Figure 5 provides the key to this problem, and in Figures 10 and 11 an idealized schematic view of these interactions is given. The energy levels in Figures 10 and 11 are a simplification of those found in Figure 5; certainly the Mn d-orbitals are not degenerate. The relative energies are assigned in accord with the trend discussed earlier (see also Figure 5) wherein the μ_3-O 2p-orbitals are lower in energy than the μ_3-Cl 3p-orbitals, as are the Mn^{IV} 3d-orbitals relative to the Mn^{III} 3d-orbitals. From Figures 10 and 11 it may be concluded that the nature of the spin donor (majority versus minority) is determined by the energy levels of the donor p-orbitals relative to the energy levels of the Mn d-orbitals; the latter are strongly spin split by spin polarization on each metal site. The rationale is that the extent of mixing and donation from

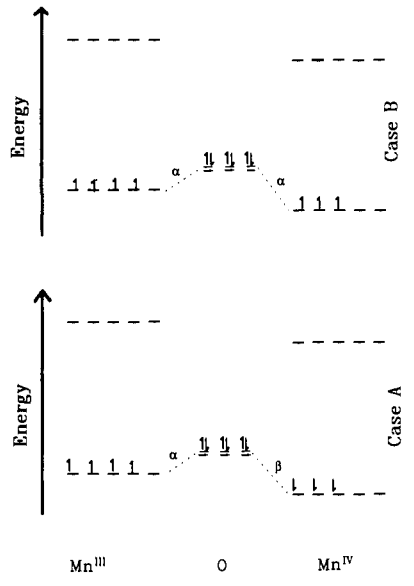

Figure 10. Simplified view of the relative energies of O^{2-} p-orbitals and those of ferromagnetically or antiferromagnetically aligned Mn^{III} and Mn^{IV} d-orbitals. The Mn designations indicate the primary metal orbitals the O^{2-} ion is expected to interact with. The spin label (α or β) indicates the predicted net spin density donated from O^{2-} to the metal orbitals.

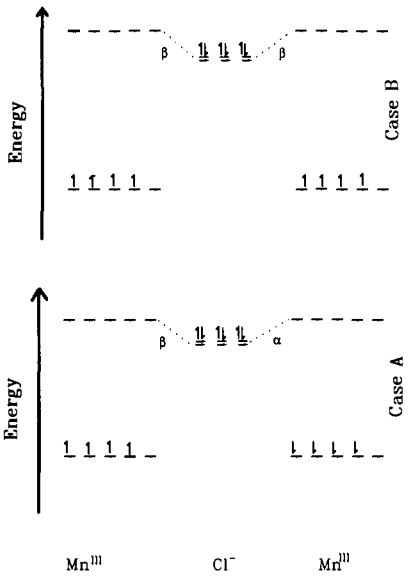

Figure 11. Simplified view of the relative energies of Cl^- p-orbitals and those of ferromagnetically (case B) or antiferromagnetically (case A) aligned Mn^{III}–Mn^{III} d-orbitals. The Mn designations indicate the primary metal orbitals the Cl^- ion is expected to interact with. The spin label (α or β) indicates the predicted net spin density donated from Cl^- to the metal orbitals.

ligand orbitals to the metal d-orbitals is greatest when the orbitals have similar energies. The most stable broken symmetry state is the $M_s = {}^9/_2$ state which corresponds to cases A and B in Figures 10 and 11, respectively. Antialignment of Mn^{III} and Mn^{IV} spin sites induces a spin polarization of the μ_3-O atom majority spin donor. Likewise, the alignment of Mn^{III} induces a spin polarization of the μ_3-Cl atom which is a minority spin donor. Flipping the Mn^{IV} spin in going from $M_s = {}^9/_2$ to $M_s = {}^{15}/_2$ has the effect of removing most of the spin polarization on all three μ_3-O atoms. It appears that in the $M_s = {}^{15}/_2$ broken symmetry state the Mn^{III} and Mn^{IV} ions are all competing for the α spin density donated by the three μ_3-O atoms. The net result is little or no spin polarization due to μ_3-O ligand spin polarization. Flipping a Mn^{III} spin in going from the $M_s = {}^9/_2$ to the $M_s = {}^1/_2$ state has the effect of lowering the net Mulliken spin population of two of the three μ_3-O atoms; from Figure 8, it is seen that there are prominent regions of both excess α and excess β density on two of three μ_3-O atoms, which probably leads to a loss in energetic stabilization.

The capping μ_3-Cl atom likely plays a role in spin-coupling strength as well. Displacement of the capping μ_3-Cl atom so that the Mn^{III}–μ_3-Cl bond length is 0.2 Å longer produces a small decrease in the magnitudes of both the J_{34} and J_{33} coupling constants by about 5 and 3 cm^{-1}, respectively. Substitution of μ_3-OH^- for μ_3-Cl^- has a much larger effect, which is strongly dependent on the Mn^{III}–(OH) distance. This and other effects of ligand substitutions, additions, and removal from this Mn_4O_3Cl cubane will be the subject of a future paper. The μ_3-Cl atom spin density for the $M_s = {}^1/_2$ case is considerably smaller (0.023) than for $M_s = {}^{15}/_2$ (0.186) and $M_s = {}^9/_2$ (0.134) broken symmetry states.

Although the change in μ_3-Cl atom spin population on going from $M_s = {}^{15}/_2$ to $M_s = {}^9/_2$ is counterintuitive since the μ_3-Cl bridges the three Mn^{III} ions, while it is the Mn^{IV} site vector that is flipped, that it occurs suggests that the spin-coupling interactions are quite complex. There are probably cooperative effects among the different ligands with respect to spin donation with corresponding effects on spin-coupling energies as well. Clearly, there are compensating effects from the majority spin donating μ_3-O ligands, and the other ligands which are mainly minority spin donors. From this perspective, even the terminal ligands may exert an influence on the spin coupling. Further analysis of the spin-coupling mechanism in this system employing alteration of the cluster composition and fragment analysis will be helpful in separating out both cooperative and noncooperative effects. For example, the effects of ligand removal or substitution and protonation/deprotonation will be explored in the tetranuclear complexes and will be compared also with the properties of simpler dinuclear systems.

The $Mn^{III,IV}$ ions can be thought of as functioning like Lewis acids, but with varying amounts of α and β spin density and net electron density being donated from various ligands. Because of the many different α and β donors to a given Mn site, and because the ideal Mn spin populations are quite high, it is very difficult to trace the detailed spin acceptance by a given Mn site. This is why we have focused largely on spin donation from idealized (initially diamagnetic) O^{2-}, Cl^-, and $(CH_3COO)^-$ groups. This is simply a particular choice of reference point which is conceptually valuable. The recently developed capability to perform fragment energy analysis using spin-polarized fragments with the Amsterdam density functional LCAO codes should provide an advantage in future work.

Comparison with Reduced $Fe_4S_4^+$ and $Fe_4Se_4^+$ Clusters. The Mn_4O_3Cl cubane cluster spin-coupling behavior can be related most closely to that of reduced $Fe_4S_4^+$ and $Fe_4Se_4^+$ clusters,[4,5,47,48] since the site spins and the possible final spin states are analogous, though not identical. For the Mn cluster, the three Mn^{III} sites have $S_1 = S_2 = S_3 = 2$, and the Mn^{IV} site has $S_4 = {}^3/_2$; the FeS and FeSe cubanes have three Fe^{II} sites with $S_1 = S_2 = S_3 = 2$, and one Fe^{III} site with $S_4 = {}^5/_2$. While the most typical total spin states for $Fe_4S_4^+$ clusters are $S = {}^1/_2$ or $S = {}^3/_2$,[4,5] for selenium-substituted $Fe_4Se_4^+$ clusters in reduced clostridial ferredoxin proteins, it is typical to have coexisting $S = {}^1/_2$, ${}^3/_2$, and ${}^7/_2$ ground states.[47,48] The $S = {}^7/_2$ state here is similar to the Mn_4O_3Cl cubane $S = {}^9/_2$ ground state since there is parallel coupling of the three $S_i = 2$ site spin vectors to give $S_A = 6$ and antiparallel coupling to the fourth spin site $S_4 = {}^3/_2$ for the Mn cubane, and $S_4 = {}^5/_2$ for the FeSe cubane. The Mn and FeSe cubanes differ in that the Mn cubane ground state in the present complex (and other similar ones) is well separated from excited spin states, and even the lowest lying excited Mn cubane spin states have a rather similar spin-coupling pattern to the ground state with $S_A = 5$ and 6. By contrast, the three coexisting FeSe cubane ground states

(47) (a) Auric, P.; Gaillard, J.; Meyer, J.; Moulis, J. M. *Biochem. J.* **1987**, *242*, 525. (b) Gaillard, J.; Moulis, J. M.; Auric, P.; Meyer, J. *Biochemistry* **1986**, *25*, 464. (c) Moulis, J. M.; Auric, P.; Gaillard, J.; Meyer, J. *J. Biol. Chem.* **1984**, *259*, 11396.

(48) (a) Noodleman, L. *Inorg. Chem.* **1991**, *30*, 246. (b) Noodleman, L. *Inorg. Chem.* **1991**, *30*, 256.

exhibit quite different spin-coupling patterns, with a wide variation in S_A = 2, 3, 4, or 6. The principal difference here is that the Mn cubane has well-defined trapped valence with distinct Mn^{III},Mn^{IV} sites and is well described by the two Heisenberg parameters J_{33} and J_{34}. Variation of the J_{33}/J_{34} ratio can lead to different spin ground states (exhibiting spin frustration), but still there is less sensitivity than in polynuclear FeS (FeSe) systems. The FeS and FeSe cubane complexes have resonance valence delocalization in addition to possibly different J parameters for $2Fe^{2+}$ and Fe^{3+}–Fe^{2+} interactions, and there is extreme sensitivity of the system ground spin state to small perturbations of geometry and electrostatic and/or solvent environment.

One interesting question arising from the comparisons above is what would be the necessary conditions for valence delocalization in dinuclear or polynuclear Mn complexes. For the present Mn_4O_3Cl cubane complex, there is very little tendency for Mn^{3+},Mn^{4+} valence delocalization to $Mn^{3.5+}$,$Mn^{3.5+}$ because the Mn^{IV} carboxylate oxygen and three μ_3-O atom environment differs in too drastic a way from the Mn^{III} environment of $2Cl_t$, 1 μ_3-Cl, 2 μ_3-O, and one carboxylate oxygen atom. This is evident since the $M_s = {}^1/_2$ broken symmetry state has parallel spin $Mn^{III}{}_a$ and Mn^{IV} sites which would show valence delocalization if this were energetically favorable, yet the net site spin and charge populations in Table IV show no valence delocalization at all. (Note that both $Mn^{III}{}_{a,b}$ have nearly the same charge as well as spin magnitudes despite the parallel alignment of $Mn^{III}{}_a$–Mn^{IV} and opposite alignment of $Mn^{III}{}_b$–Mn^{IV}. The charge and spin magnitude of Mn^{IV} is very different.) Such valence delocalization would be of more than academic interest. In addition to its importance in determining the spin ground state of the system, valence delocalization or alternation between delocalized and trapped valence with changes in coordination environment provides a method for facilitating charge separation between metal sites on the cluster and nearby acceptor as might occur in the interaction of the water oxidation complex with its electron acceptor (tyrosine Y_Z). Even if true valence delocalization does not occur, facile valence alternation and interconversion would be favorable for such charge separation; this could be achieved, for example, by coordinating changes in Mn–carboxylate oxygen geometry with Mn valence interconversion.

Conclusion

There are a number of important conclusions from our results. (1) It is possible to calculate the magnetic properties of a weakly interacting polynuclear Mn cluster by combining spin-polarized density functional LCAO and broken symmetry methods. Further, we have done this successfully in a tetranuclear cluster where the relevant energy differences are one-third to one-tenth of those in corresponding polynuclear FeS clusters. We note also that a rather complicated Heisenberg spin ladder (Figure 3) is readily derived from a few broken symmetry state energy differences. (2) In our complex and probably also in related systems including the water oxidation center (WOC) [equivalently, the oxygen evolving complex (OEC)] of photosystem II, ligand spin polarization is an important mechanism in the stabilization of particular spin states. In the present complex, the Mn–μ_3-O–Mn interaction is most important. There may also be contributions to the spin coupling from the other bridging and terminal ligands; there are indications that some of these interactions can be cooperative. While the influence of superexchange interactions is not entirely excluded, ligand spin polarization plays the more important role in spin coupling. (3) The nature and extent of ligand spin polarization and spin donation are controlled by the relative energies of the active metal and ligand orbitals. In systems with less than a half-filled 3d shell, both majority spin and minority spin donation by the ligands is possible, and these may interact in a complicated way. In this manner, $Mn^{III,IV}$ complexes (<half-filled) differ in a major way from $Fe^{II,III}$ and Cu^{II} complexes. (4) The ligand environments around the Mn^{III} and Mn^{IV} sites in the present $[Mn_3O_3(OAc)_3Cl_7]^{3-}$ complex are too different to allow resonance valence delocalization with its associated spin coupling as found in polynuclear FeS complexes. However, in the presence of a more symmetric (or more labile) ligand environment, valence delocalization for mixed valence MnO dinuclear or polynuclear complexes may be possible, as found recently in one FeO dimer complex. It is possible that either valence delocalization or valence interconversion is involved in keeping charges separated in the initial oxidation steps of the OEC. Experimental evidence bearing on this question should be explored.

As discussed in the Introduction, the S_2 state of the OEC has either an $S = {}^1/_2$ or $S = {}^3/_2$ ground state. The particular complex studied here and similar complexes have $S = {}^9/_2$ ground states, which makes them unlikely models for the S_2 state of the OEC. $Mn^{III}{}_3Mn^{IV}$ complexes of C_3 symmetry can in principle have any ground state within the range $S = {}^{15}/_2$–${}^1/_2$ depending on the values of J_{34} and J_{33}. (Similar general considerations apply in lower symmetry, although with more J parameters.) Therefore either ligand substitution, geometric distortion, or possibly a different coordination geometry such as a butterfly arrangement is necessary to achieve congruence between a chemical model system and the actual S_2 state of the OEC. One of our future goals will be to examine how the spin ground state in tetranuclear and simpler dinuclear MnO complexes varies as a function of coordination geometry, cluster composition, and oxidation state. This should also provide us with further insight into the mechanism of spin coupling.

It is also very important to follow the flow of charge in different clusters. We note that even the present cubane complex contains the same type of bridging and terminal ligands as are thought to be present in the WOC, particularly μ-O and carboxylate oxygens, and possibly Cl. Of course, H_2O's are also present as ligands at some stage of the oxidation cycle, although it is not clear whether H_2O coordination is present already at the S_2 step. The rather strong Mn–μ-O covalency, μ-O Mulliken charge of about –0.7, displayed in our calculations is suggestive of coordinated H_2O or μ-O ligands in transition to molecular oxygen. Far more needs to be done both experimentally and theoretically before we will attain a good understanding of the OEC cycle.

Acknowledgment. We are grateful for partial funding from NIH Grant HL13652 (D.N.H.). At Scripps, this work was supported by NIH Grant GM43278 to L.N. We thank Peter Vernooijs for technical assistance on the DF-LCAO calculations and Mike Pique for his work on the computer graphics.

Supplementary Material Available: Tables of atomic coordinates for $[Mn_4O_3Cl_7(O_2CCH_3)_6]^{3-}$, Slater orbital basis functions used in calculations, molecular orbital energies, and composition (23 pages). Ordering information is given on any current masthead page.